International Journal of Heat and Mass Transfer 273 (2027) 129679

Contents lists available at ScienceDirect

International Journal of Heat and Mass Transfer

journal homepage: www.elsevier.com/locate/hmt

Thermal and radiative properties of $BaZrO_3$ and $Gd_2Zr_2O_7$ for thermal barrier coating applications: A first-principles study

Harish Kumar [a], Sreerag Sundaram [a], Ankit Jain [b], Karthik Sasihithlu [a,*]

[a] Department of Energy Science and Engineering, Indian Institute of Technology Bombay, Powai, Mumbai 400076, India
[b] Department of Mechanical Engineering, Indian Institute of Technology Bombay, Powai, Mumbai 400076, India

ARTICLE INFO

Keywords:
Thermal barrier coatings
First-principles calculations
Four-phonon scattering
Radiative thermal conductivity
High-temperature heat transport

ABSTRACT

$BaZrO_3$ and $Gd_2Zr_2O_7$ are promising thermal barrier coating materials owing to their high-temperature stability and low thermal conductivity. In this work, the temperature-dependent thermal conductivity of $BaZrO_3$ and $Gd_2Zr_2O_7$ is investigated from first-principles by combining lattice and radiative heat-transport mechanisms. The lattice thermal conductivity is evaluated by accounting for both particle-like and coherent phonon transport, with the particle-like contribution calculated using temperature-dependent interatomic force constants and including both three- and four-phonon scattering processes, and the coherent contribution evaluated using the Wigner transport formalism. The radiative contribution is evaluated from temperature-dependent optical properties within the Rosseland approximation. Inclusion of four-phonon scattering significantly reduces the particle-like lattice thermal conductivity, while the coherent contribution increases with temperature and becomes comparable to the particle-like contribution in $Gd_2Zr_2O_7$ at elevated temperatures. Radiative heat transport also becomes increasingly significant at high temperatures, contributing substantially to the overall thermal conductivity. The combined particle-like, coherent and radiative transport framework provides a more accurate description of the experimentally observed high-temperature behavior than phonon-only calculations, highlighting the importance of multiple heat-transport channels in these oxide ceramics.

1. Introduction

The development of high-performance gas-turbine engines is increasingly driven by the need for higher gas-inlet temperatures, which are presently approaching 1700°C, in order to improve operating efficiency. To protect metallic turbine components under such severe conditions, thermal barrier coatings (TBCs) are employed to provide thermal resistance and preserve structural integrity [1–3]. Materials used for TBCs are typically refractory ceramics with intrinsically low thermal conductivity [4]. In addition, they should possess a high melting point, a high thermal expansion coefficient, damage tolerance, and good high-temperature mechanical stability [5]. The most widely used TBC material is 6%–8% yttria-stabilized zirconia (YSZ) [6]. However, the performance of YSZ deteriorates above 1200°C owing to phase transformations and rapid sintering [7]. This limitation has motivated the search for alternative oxide ceramics that can retain low thermal conductivity and structural stability at higher operating temperatures.

Several families of materials have been identified as potential candidates for TBCs, including ABO_3-type perovskites and rare-earth pyrochlores with the general formula $A_2B_2O_7$. These materials offer broad compositional flexibility and diverse crystal structures, and particularly, perovskite zirconates [8,9] and rare-earth zirconates [10] have shown promising high-temperature thermal properties. Among the perovskite zirconates, $BaZrO_3$ has emerged as a promising TBC material owing to its high melting point, excellent chemical stability, favorable thermophysical properties, and low thermal conductivity [7,11,12]. Previous theoretical and experimental studies on $BaZrO_3$ have examined its structural stability, elastic behavior, thermophysical properties, and lattice thermal transport at elevated temperatures, highlighting the important role of anharmonicity in governing phonon transport [12,13].

Similarly, rare-earth zirconates, particularly $Gd_2Zr_2O_7$, have been widely investigated as next-generation TBC materials owing to their intrinsically low thermal conductivity, excellent phase stability at elevated temperatures, superior resistance to calcium–magnesium–alumino–silicate (CMAS) attack, reduced sintering, and improved environmental durability [7,14–16]. Experimental and theoretical studies on $Gd_2Zr_2O_7$ have primarily focused on thermophysical properties, temperature-dependent thermal conductivity using molecular dynamics

* Corresponding author.
E-mail address: ksasihithlu@ese.iitb.ac.in (K. Sasihithlu).

https://doi.org/10.1016/j.ijheatmasstransfer.2026.129679
Received 2 July 2026; Received in revised form 10 September 2026; Accepted 26 September 2026
Available online 9 October 2026
0017-9310/© 2026 Elsevier Ltd. All rights are reserved, including those for text and data mining, AI training, and similar technologies.

simulations, phase stability, thermal cycling behavior, and compositional engineering through rare-earth substitution to improve thermal insulation and environmental durability [15,17–22].

At moderate temperatures, heat transport in ceramic TBCs is generally dominated by phonons, and the lattice thermal conductivity usually decreases with increasing temperature because of enhanced phonon scattering. Several theoretical studies have examined lattice thermal transport in TBC materials; however, thermal conductivity calculations are often limited to lower-order anharmonic approximations and primarily consider three-phonon scattering processes [12,20]. Recent investigations have shown that temperature-induced phonon renormalization and higher-order anharmonic interactions, particularly four-phonon scattering with particle like and wave-like thermal transport, can substantially alter phonon frequencies, scattering phase space, and phonon lifetimes, thereby significantly influencing lattice thermal conductivity at elevated temperatures in strongly anharmonic TBC materials [13,23]. At sufficiently high temperatures, radiative heat transfer can also become important. When temperatures exceed approximately 1500°C, ceramic materials can emit thermal radiation in the visible and near-infrared regions of the electromagnetic spectrum, where many TBC materials are partially transparent. Since radiative heat transfer scales strongly with temperature, approximately as T^4, it can become a significant contribution to the effective thermal conductivity at elevated temperatures [24]. Recent first-principles studies have highlighted the importance of accounting for radiative transport alongside phonon-mediated heat conduction in refractory ceramics and TBC materials [25,26]. Experimental investigations have further demonstrated that microstructural engineering can effectively suppress radiative heat transfer by enhancing infrared scattering and reducing transmissivity [27]. However, experimental determination of radiative thermal properties is also challenging because it requires precise temperature control, accurate separation of sample radiation from background radiation, and reliable high-temperature optical measurements. As a result, direct measurements of radiative heat transfer and radiative material properties remain limited [24]. These challenges motivate first-principles approaches that can predict both lattice and radiative contributions to the thermal conductivity of candidate TBC materials.

In this study, we investigate thermal transport in pure bulk crystals of $BaZrO_3$ and $Gd_2Zr_2O_7$ by calculating both lattice and radiative contributions to thermal conductivity. The calculations are carried out over 300–2800 K for $BaZrO_3$ and 300–1800 K for $Gd_2Zr_2O_7$, consistent with their respective high-temperature stability ranges. The lattice thermal conductivity is calculated by solving the phonon Boltzmann transport equation (BTE), explicitly considering temperature renormalization, three- and four-phonon scattering processes, and the non-diagonal, coherent contribution to the thermal transport. The radiative contribution is quantified using the Rosseland approximation, with the required temperature-dependent optical properties predicted from first-principles calculations.

Previous studies on $BaZrO_3$ [12,13] have primarily focused on lattice thermal transport, while studies on $Gd_2Zr_2O_7$ have either considered only lattice thermal transport [20] or have included radiative contributions using simplified optical models [28]. Consequently, a unified first-principles description of high-temperature heat transport accounting simultaneously for higher-order anharmonic phonon scattering and temperature-dependent radiative transfer remains lacking. By combining temperature-renormalized phonon transport with first-principles, temperature-dependent thermo-optical properties, the present work provides a more comprehensive description of thermal transport in $BaZrO_3$ and $Gd_2Zr_2O_7$, and enables their assessment as candidate materials for next-generation thermal barrier coatings.

2. Calculation methods

2.1. First-principles calculations

All first-principles calculations were performed using the Vienna Ab initio Simulation Package (VASP) within the framework of density functional theory (DFT) [29]. To describe the electron-ion interactions the projector augmented wave (PAW) method [30] was employed, and the exchange–correlation functional was treated using the generalized gradient approximation (GGA) in the Perdew–Burke–Ernzerhof implementation revised for solids (PBEsol) [31]. For $BaZrO_3$, the electronic energy convergence criterion, force convergence criterion for structural relaxation, and plane-wave cutoff energy were set to 10^{-8} eV, 10^{-6} eV Å^{-1}, and 500 eV, respectively. For $Gd_2Zr_2O_7$, the corresponding values were 10^{-8} eV, 10^{-3} eV Å^{-1}, and 600 eV. The electronic energy convergence criterion and plane-wave cutoff energy were used in both structural relaxation and interatomic force constant (IFC) calculations, whereas the force convergence criterion was applied only during structural relaxation. The Brillouin zone was sampled using Monkhorst–Pack meshes [32] of $6 \times 6 \times 6$ for $BaZrO_3$ and $4 \times 4 \times 4$ for $Gd_2Zr_2O_7$. The convergence of the total energy with respect to the plane-wave cutoff energy and k-point mesh is shown in Figs. S1 and S2, respectively, in the Supplementary Information. Both lattice parameters and atomic positions were fully relaxed until convergence criteria was satisfied. To accurately account for the strong on-site Coulomb interactions associated with the localized Gd-4f states in $Gd_2Zr_2O_7$, the Hubbard-U correction within the DFT+U formalism proposed by Dudarev [33] was applied. The effective Hubbard parameter for Gd was taken as $U_{\mathrm{eff}} = 6.9$ eV as proposed by Losovyj et al. [34] for Gd_2O_3. Born effective charges were calculated using density functional perturbation theory (DFPT) [35] and were subsequently used in the calculation of infrared optical properties.

2.2. Temperature-dependent interatomic force constants and phonon dispersion spectra

Temperature-dependent interatomic force constants (IFCs) were obtained using the stochastic sampling approach implemented in the TDEP package [36]. Thermally displaced configurations were generated using the *canonical_configuration* module [37], and DFT-calculated forces on these configurations were subsequently used to fit temperature-dependent second-order [38], third-order [39], and fourth-order IFCs [40], thereby incorporating finite-temperature phonon renormalization effects. For $BaZrO_3$, a $3 \times 3 \times 3$ supercell and a $2 \times 2 \times 2$ Monkhorst–Pack k-point mesh were used for the IFC calculations. For $Gd_2Zr_2O_7$, with unit cell comprising 88 atoms, the IFC calculations were performed using the conventional unit cell ($1 \times 1 \times 1$ supercell) and a $4 \times 4 \times 4$ Monkhorst–Pack k-point mesh. For lattice thermal conductivity and optical properties calculation, $12 \times 12 \times 12$ and $8 \times 8 \times 8$ q-grid meshes were used for $BaZrO_3$ and $Gd_2Zr_2O_7$, respectively. The convergence of the lattice thermal conductivity with respect to the q-grid mesh is shown in Fig. S3 in the Supplementary Information. The cutoff radii for fitting the second-, third-, and fourth-order IFCs were chosen as 6.35 Å, 5.0 Å, and 5.0 Å, respectively, for $BaZrO_3$. For $Gd_2Zr_2O_7$, the corresponding cutoff radii were 5.24 Å, 4.5 Å, and 4.0 Å. These cutoff radii were chosen according to the interaction ranges recommended by the TDEP framework for the adopted supercells, with the largest recommended values being adopted in each case. The temperature-dependent second-order IFCs were used to calculate vibrational properties (phonon dispersion spectra and density of states) at finite temperatures, ensuring a self-consistent description of phonon frequencies, eigenvectors, and group velocities for both materials.

2.3. Lattice thermal conductivity

The lattice thermal conductivity was evaluated within a multichannel phonon transport framework that accounts for both particle-like and wave-like heat transport using the unified thermal transport theory [41]. The particle-like contribution, κ^{P}, was obtained by solving the Peierls–Boltzmann transport equation, while the wave-like coherent

contribution, κ^{C}, was evaluated using the Wigner phase-space formalism [41,42]. In this framework, the coherent contribution arises from the off-diagonal elements of the phonon distribution and describes heat transfer between different vibrational eigenstates. The particle-like and coherent contributions to the lattice thermal conductivity, κ_L, are expressed as follows:

$$\kappa_{L}^{P/C} = \frac{\hbar^2}{k_B T^2 V N} \sum_{\mathbf{q}} \sum_{j,j'} \frac{\omega_{\mathbf{q}j} + \omega_{\mathbf{q}j'}}{2} v^{\alpha}_{\mathbf{q}jj'} \otimes v^{\beta}_{\mathbf{q}j'j} \times \frac{\omega_{\mathbf{q}j} n_{\mathbf{q}j} \left(n_{\mathbf{q}j}+1\right) + \omega_{\mathbf{q}j'} n_{\mathbf{q}j'} \left(n_{\mathbf{q}j'}+1\right)}{4\left(\omega_{\mathbf{q}j} - \omega_{\mathbf{q}j'}\right)^2 + \left(\Gamma_{\mathbf{q}j} + \Gamma_{\mathbf{q}j'}\right)^2} \times \left(\Gamma_{\mathbf{q}j} + \Gamma_{\mathbf{q}j'}\right) \tag{1}$$

where the superscripts P and C represent the contributions from populations (particle-like propagation) and coherences (wave-like phonon tunneling), respectively. $\hbar$, k_B, V, N, v, and Γ denote reduced Planck constant, Boltzmann constant, volume of the unit cell, number of sampled phonon wave vectors in the first Brillouin zone, phonon group velocity, and phonon scattering rates, respectively. n represents the equilibrium Bose–Einstein distribution, $n_{\mathbf{q}j} = [\exp(\hbar\omega_{\mathbf{q}j}/k_B T) - 1]^{-1}$, [23] where $\omega_{\mathbf{q}j}$ is the phonon angular frequency. When $j = j'$, Eq. (1) yields the population (particle-like) contribution corresponding to the Peierls–Boltzmann transport description whereas the $j \neq j'$ terms give the coherent (wave-like) contribution. The coherent contribution becomes relevant when the frequency separation between phonon modes is comparable to their linewidths and the corresponding off-diagonal velocity matrix elements are appreciable. Thus, phonon modes satisfying $\left|\omega_{\mathbf{q}j} - \omega_{\mathbf{q}j'}\right| \lesssim \Gamma_{\mathbf{q}j} + \Gamma_{\mathbf{q}j'}$ can contribute significantly to κ^{C}.

The total lattice thermal conductivity was subsequently obtained by summing the particle-like and coherent transport channels:

$$\kappa_L = \kappa^{P} + \kappa^{C} \tag{2}$$

The phonon scattering rates required for the evaluation of κ_L in Eq. (1) were calculated within the relaxation-time approximation using the FourPhonon module [43] developed on the ShengBTE framework [44]. The three- and four-phonon scattering rates were evaluated using a sampling-based maximum-likelihood estimation approach [45], in which a representative subset of scattering processes is sampled to estimate the total scattering rate, thereby reducing computational cost while retaining accuracy. In the present work, 10^6 scattering processes were sampled for both three- and four-phonon calculations. Details of the convergence with respect to the number of sampled scattering processes are given in Tables S1 and S2 in the Supplementary Information. The total phonon lifetime was obtained by combining the three- and four-phonon scattering contributions using Matthiessen's rule [46].

2.4. Optical properties

To evaluate the temperature-dependent optical properties required for the radiative thermal conductivity calculations, the infrared dielectric response was computed from first-principles following the approach described in Ref. [47]. In this framework, the infrared optical response is described through the interaction of electromagnetic radiation with the infrared-active transverse optical (TO) phonon modes near the Brillouin zone center, leading to the following expression for the complex dielectric tensor:

$$\varepsilon_{\mu\nu}(\omega, T) = \varepsilon_{\infty} + \frac{4\pi}{\hbar V_{\text{cell}}} \times \sum_{0j} \frac{S^{j}_{\mu\nu}(T)}{\omega^2_{0,j}(T) - \omega^2 + 2\omega_{0,j}(T)\Sigma_j(\omega_{0,j}, T)} \tag{3}$$

where $\omega_{0,j}$ is the frequency of the jth infrared-active TO phonon mode, $S^{j}_{\mu\nu}$ is the oscillator strength tensor, and $\Sigma_j(\omega, T) = \Delta_j(\omega, T) - i\Gamma_j(\omega, T)$ is the phonon self-energy. The real and imaginary parts of the phonon self-energy, $\Delta_j(\omega, T)$ and $\Gamma_j(\omega, T)$, are related through the Kramers–Kronig transformation. Their values evaluated at the resonant frequencies of the infrared-active modes account for the temperature-dependent frequency renormalization and linewidth broadening of the infrared resonances, respectively. Notably, the phonon damping factors Γ_j entering the dielectric response are obtained from the same anharmonic phonon scattering calculations used in the thermal-conductivity analysis, providing a direct link between lattice thermal transport and the temperature-dependent optical properties. The oscillator strength $S^{j}_{\mu\nu}$ is calculated from the Born effective charges Z^*, atomic masses m_κ, and phonon eigenvectors $e_{\kappa\mu}$ as:

$$S^{j}_{\mu\nu} = \left(\sum_{\kappa\mu'} Z^{*}_{\kappa,\mu\mu'} \frac{e_{\kappa\mu'}(0j)}{\sqrt{m_\kappa}}\right)\left(\sum_{\kappa\nu'} Z^{*}_{\kappa,\nu\nu'} \frac{e_{\kappa\nu'}(0j)}{\sqrt{m_\kappa}}\right) \tag{4}$$

The real and imaginary parts of the complex refractive index, $n(\omega, T)$ and $k(\omega, T)$, respectively, were subsequently obtained from the complex dielectric function through the relation:

$$n(\omega, T) + ik(\omega, T) = \sqrt{\varepsilon(\omega, T)}. \tag{5}$$

The infrared optical response considered in the present work arises from resonant interactions between electromagnetic radiation and infrared-active phonons. Since the phonon spectrum of oxide ceramics typically extends up to frequencies of the order of 10–30 THz [48,49], the first-principles optical model was employed over the frequency range 1–100 THz. In wavelength terms, this corresponds to wavelengths longer than approximately 3 μm.

At temperatures above approximately 800 K, the blackbody emission spectrum shifts towards shorter wavelengths, and a non-negligible fraction of the radiative energy lies in the near-infrared (NIR) region. In this spectral range, both $BaZrO_3$ and $Gd_2Zr_2O_7$ are reported to exhibit low absorption coefficients and high transparency, with only weak wavelength dependence of absorption [50–52]. Therefore, for wavelengths shorter than 3 μm, the spectral absorption coefficient was approximated, at each temperature, by its calculated value near 3 μm and assumed to be wavelength independent in this spectral region. The corresponding imaginary part of the complex refractive index $k(\omega, T)$ was determined from this absorption coefficient to ensure continuity with the calculated optical response at 3 μm.

2.5. Radiative thermal conductivity

For an optically thick ceramic medium, where the characteristic radiative transport length is sufficiently smaller than the coating thickness, radiative heat transfer can be approximated as a diffusion process and represented through an effective temperature-dependent radiative thermal conductivity. This treatment corresponds to the Rosseland diffusion approximation, in which the radiative transfer equation is reduced to a diffusion-like form for the radiative heat flux [24,53]. Within the Rosseland approximation, the radiative thermal conductivity $\kappa_{\text{rad}}(T)$ is expressed as

$$\kappa_{\text{rad}}(T) = \frac{16 n^2(T) \sigma T^3}{3\beta_R(T)} \tag{6}$$

where σ is the Stefan–Boltzmann constant, $n(T)$ is the effective refractive index, and $\beta_R(T)$ is the Rosseland mean extinction coefficient. Since the materials considered in this study are pure bulk crystals, the calculated optical response represents only the intrinsic absorption and excludes scattering effects arising from pores, grain boundaries, cracks, or other microstructural features. Therefore, the spectral extinction coefficient entering the Rosseland treatment is approximated as $\beta(\omega, T) = \alpha(\omega, T)$. Consequently, $\beta_R(T)$ calculated in the present work represents an absorption-based Rosseland mean extinction coefficient which is obtained as:

$$\frac{1}{\beta_R(T)} = \int_0^{\infty} \frac{1}{\alpha(\omega, T)} \frac{\partial E_{b\omega}}{\partial E_b} d\omega \tag{7}$$

where $\alpha(\omega, T) = 2\omega k(\omega, T)/c$ is the spectral absorption coefficient, $E_{b\omega}$ is the spectral blackbody emissive power, and E_b is the total

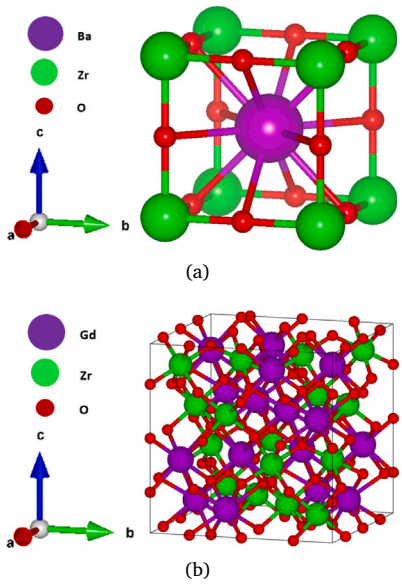

Fig. 1. Crystal structures of $BaZrO_3$ and $Gd_2Zr_2O_7$.

hemispherical blackbody emissive power, and the normalized spectral weighting function $\partial E_{b\omega}/\partial E_b$ is obtained from:

$$\frac{\partial E_{b\omega}}{\partial E_b} \equiv \frac{\partial E_{b\omega}/\partial T}{\partial E_b/\partial T}; \tag{8}$$

The effective refractive index appearing in Eq. (6) is obtained as the blackbody-weighted spectral average

$$n(T) = \int_0^\infty n(\omega, T)\, \frac{\partial E_{b\omega}}{\partial E_b}\, d\omega \tag{9}$$

3. Results and discussion

3.1. Structural and vibrational properties

The optimized crystal structures of $BaZrO_3$ and $Gd_2Zr_2O_7$ are shown in Fig. 1. $BaZrO_3$ crystallizes in the cubic perovskite structure with space group $Pm\bar{3}m$ and contains five atoms in the primitive unit cell, as shown in Fig. 1(a). The relaxed lattice parameter obtained from the present DFT calculations is 4.234 Å, which is in good agreement with the reported experimental value of approximately 4.23 Å [12]. $Gd_2Zr_2O_7$ crystallizes in the cubic pyrochlore structure with space group $Fd\bar{3}m$, as illustrated in Fig. 1(b). The conventional unit cell contains 88 atoms. The optimized lattice parameter obtained in the present work is 10.488 Å, which compares well with the experimentally reported value of 10.540 Å [54].

The calculated phonon density of states (DOS) for $BaZrO_3$ and $Gd_2Zr_2O_7$ at 300 K and 1500 K are shown in Figs. 2(a) and 2(b), respectively. Although the overall spectral features remain largely preserved with increasing temperature, noticeable shifts in peak positions and changes in peak intensities are observed for both materials, indicating finite-temperature phonon renormalization and anharmonic effects. The absence of imaginary modes or significant phonon softening confirms the dynamical stability of both materials over the investigated temperature range. The corresponding phonon dispersion curves at 300 K and 1500 K are provided in Fig. S4 in the Supplementary Information.

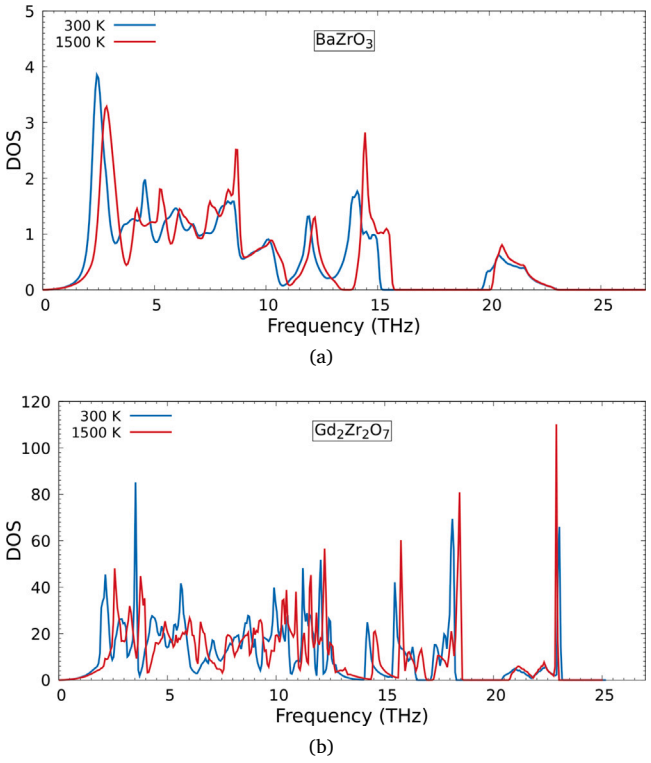

Fig. 2. Calculated density of states (DOS) of (a) $BaZrO_3$ and (b) $Gd_2Zr_2O_7$ at 300 K and 1500 K.

3.2. Lattice thermal conductivity

The temperature-dependent particle-like lattice thermal conductivities (κ^P) of $BaZrO_3$ and $Gd_2Zr_2O_7$, calculated from first-principles using the methodology described in Section 2.3, are presented in Figs. 3(a) and 3(b), respectively, together with the corresponding experimental data reported in the literature. For $Gd_2Zr_2O_7$, the experimental values shown in Fig. 3(b) are corrected for the reported sample porosity (~10%) using the Klemens relation, as described in Ref. [28]. For both materials, the particle-like contribution decreases with increasing temperature, reflecting the progressive enhancement of phonon–phonon scattering (details are given in the Figs. S5 and S6 in the Supplementary Information.)

For $BaZrO_3$, the calculation considering only three-phonon scattering overestimates the lattice thermal conductivity at lower temperatures. The inclusion of four-phonon scattering substantially reduces κ^P and improves the agreement with the experimental data in this temperature range. At room temperature, the calculated κ^P including both three- and four-phonon scattering is approximately 6.43 $W\,m^{-1}\,K^{-1}$, compared with the experimental value of 5.72 $W\,m^{-1}\,K^{-1}$ [12]. The reduction in κ^P upon inclusion of four-phonon scattering demonstrates the importance of higher-order anharmonic interactions in $BaZrO_3$. Nevertheless, κ^P continues to decrease with increasing temperature and becomes significantly lower than the experimentally measured thermal conductivity at elevated temperatures. A similar reduction in the particle-like thermal conductivity is observed for $Gd_2Zr_2O_7$ upon inclusion of four-phonon scattering. At room temperature, the calculated κ^P including three- and four-phonon scattering is approximately 1.53 $W\,m^{-1}\,K^{-1}$, compared with the porosity-corrected experimental value of 1.79 $W\ m^{-1}\ K^{-1}$ [28]. With increasing temperature, the particle-like contribution decreases further, reaching approximately 0.75 $W\,m^{-1}\,K^{-1}$ at 1500 K. In contrast, the experimental thermal

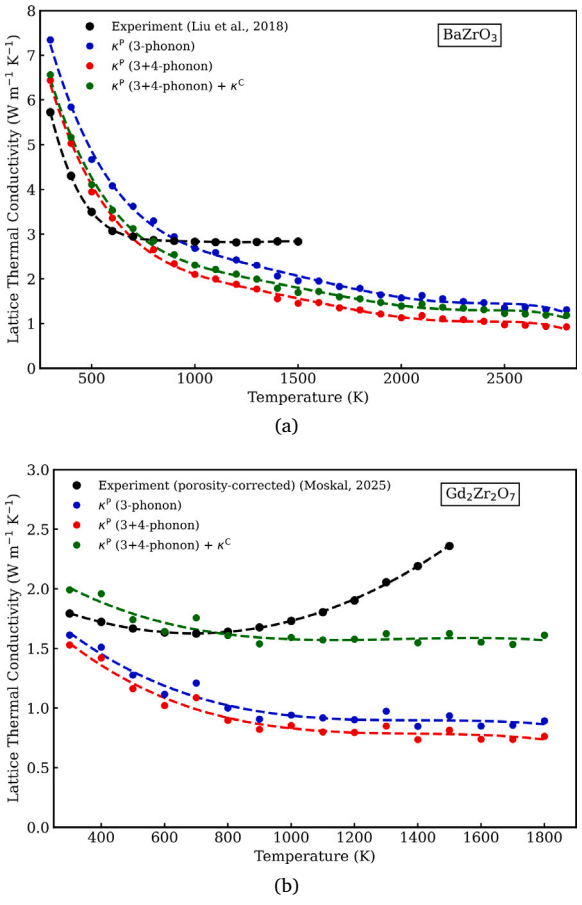

Fig. 3. Comparison of the calculated temperature-dependent lattice thermal conductivity of (a) $BaZrO_3$ and (b) $Gd_2Zr_2O_7$ with experimental results. [12, 28]. For $Gd_2Zr_2O_7$ the experimental thermal conductivity values are corrected for the reported sample porosity (~10%) using the Klemens relation, as described in Ref. [28]. Symbols represent calculated values and dashed lines correspond to polynomial fits.

conductivity initially decreases only moderately and subsequently increases above approximately 700–800 K. Consequently, the discrepancy between the particle-like contribution and the experimental thermal conductivity becomes progressively larger at elevated temperatures for both materials, indicating that particle-like phonon transport alone cannot account for the observed temperature dependence.

To investigate the origin of this deviation, the coherent contribution to lattice thermal transport, κ^C, was evaluated using the unified thermal transport formalism described in Section 2.3. The resulting total lattice thermal conductivity, $\kappa_L = \kappa^P + \kappa^C$, is also presented in Fig. 3. In contrast to the particle-like contribution, κ^C increases with temperature for both materials, indicating an increasing contribution from phonon coherences as the vibrational modes broaden with increasing phonon scattering. The relative importance of this contribution, however, differs substantially between the two materials.

For $BaZrO_3$, the coherent contribution remains small in magnitude relative to the particle-like contribution, increasing from approximately 0.12 W m^{-1} K^{-1} to approximately 0.26 W m^{-1} K^{-1} at elevated temperatures, beyond which it remains nearly temperature independent. In contrast, for $Gd_2Zr_2O_7$, κ^C is substantially larger, increasing from approximately 0.46 W m^{-1} K^{-1} at 300 K to 0.80–0.85 W m^{-1} K^{-1} at elevated temperatures. At high temperatures, the coherent contribution becomes comparable in magnitude to the particle-like contribution in $Gd_2Zr_2O_7$, demonstrating the significant role of coherent transport in its lattice thermal conductivity. The stronger coherent contribution in $Gd_2Zr_2O_7$ can be understood from its larger and more complex vibrational spectrum compared with $BaZrO_3$. The larger number of phonon branches results in a greater number of closely spaced vibrational modes, increasing the possibility of coherent coupling between different phonon states. With increasing temperature, phonon linewidth broadening further increases the overlap between closely spaced modes, thereby enhancing the coherent transport contribution. In $BaZrO_3$, which has a considerably simpler phonon spectrum, such coherence effects remain comparatively weaker.

The combined lattice thermal conductivity, $\kappa_L = \kappa^P + \kappa^C$, therefore provides a more complete description of lattice thermal transport than the particle-like contribution alone. The inclusion of κ^C partially compensates for the decrease in κ^P with increasing temperature, with this effect being particularly pronounced for $Gd_2Zr_2O_7$. These results demonstrate that, while higher-order anharmonic scattering is important for accurately describing the particle-like contribution, coherent phonon transport also becomes increasingly important at elevated temperatures. However, even after accounting for both particle-like and coherent contributions, the calculated lattice thermal conductivity remains lower than the experimentally observed thermal conductivity at elevated temperatures. This remaining discrepancy suggests the increasing importance of an additional heat-transfer mechanism at high temperatures. We therefore examine the radiative contribution in the following section.

3.3. Radiative thermal conductivity

In order to evaluate the radiative thermal conductivity using Eq. (6), the temperature-dependent optical properties of $BaZrO_3$ and $Gd_2Zr_2O_7$ were calculated following the methodology described in Section 2.4. The resulting spectra, $n(\omega, T)$ and $k(\omega, T)$, at 300 K and 1500 K are shown in Figs. 4(a) and 4(b), respectively. For $BaZrO_3$, the calculated optical response at 300 K is additionally compared with the experimentally measured optical constants reported by Gim et al. [55]. As shown in Fig. 4(a), the calculations reproduce the principal experimentally observed resonance features in both the real and imaginary parts of the complex refractive index, including their approximate frequency locations and overall spectral behavior. Some differences in the positions and magnitudes of the individual resonances are observed, which may arise from differences between the idealized first-principles description and the experimental material. Nevertheless, the comparison provides experimental support for the principal features of the calculated infrared optical response. Although optical properties over the entire 0–100 THz frequency range were used in the radiative thermal conductivity calculations, only the 0–40 THz region is presented here, as it contains the most significant temperature-dependent variations in $n(\omega, T)$ and $k(\omega, T)$. The complete temperature-dependent optical spectra over the 0–100 THz frequency range are provided in the Supplementary Information.

For both materials, the optical response is governed by infrared-active optical phonons, which give rise to characteristic resonances in both the refractive index and extinction coefficient. Increasing temperature results in broadening and modification of these spectral features, indicating enhanced anharmonic phonon interactions. Compared with $BaZrO_3$, $Gd_2Zr_2O_7$ exhibits a larger number of infrared-active modes and consequently a more complex spectral response, consistent with its larger and more complex pyrochlore crystal structure. For $Gd_2Zr_2O_7$, comparable experimental bulk optical constants over the spectral range considered here were not available for direct validation.

The radiative thermal conductivities of $BaZrO_3$ and $Gd_2Zr_2O_7$, calculated using Eq. (6), are presented in Fig. 5. For both materials, the radiative contribution increases rapidly with temperature, showing the enhanced role of photon transport at elevated temperatures. For both materials, the calculated values also exhibit an approximately cubic temperature dependence, consistent with the T^3 scaling expected from

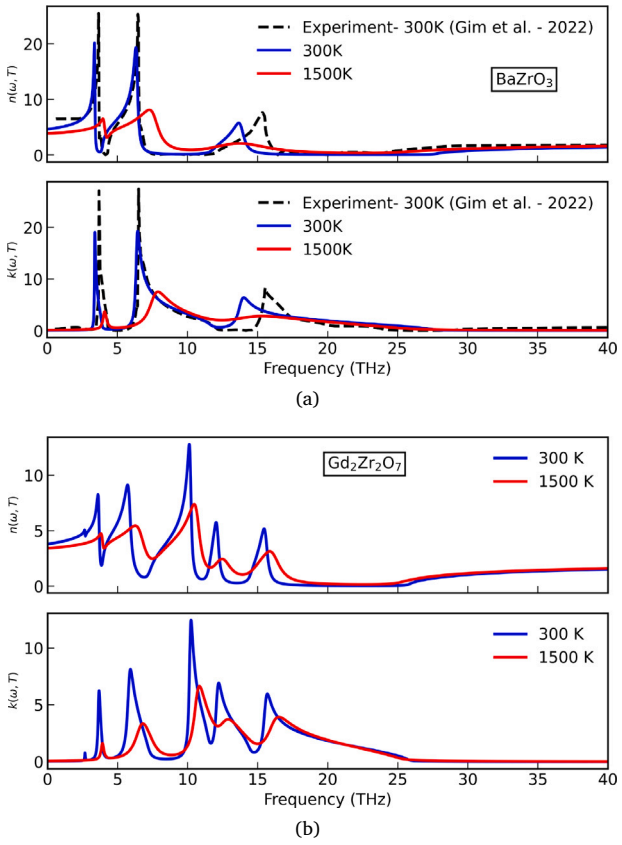

Fig. 4. Real, $n(\omega, T)$, and imaginary, $k(\omega, T)$, parts of the complex refractive index as a function of frequency for (a) $BaZrO_3$ and (b) $Gd_2Zr_2O_7$ at 300 K and 1500 K. For $BaZrO_3$, the calculated results at 300 K are compared with the corresponding experimental data measured at 300 K by Gim et al. [55].

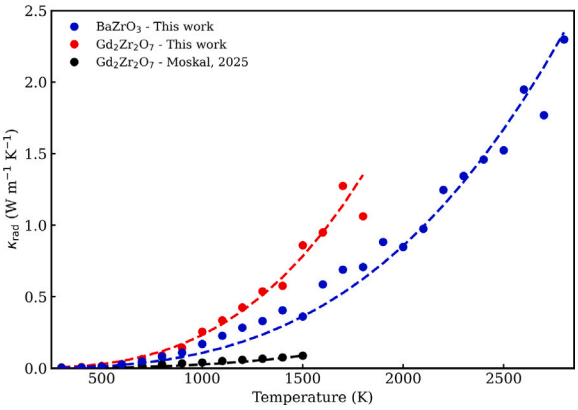

Fig. 5. Radiative thermal conductivity of $BaZrO_3$ and $Gd_2Zr_2O_7$ calculated using the Rosseland approximation. Symbols represent the calculated values, while dashed lines correspond to reference curves of the form aT^3, where a is a constant. The reference curves are included to illustrate the approximate cubic temperature dependence expected from the Rosseland approximation. For $Gd_2Zr_2O_7$, the radiative thermal conductivity reported by Moskal [28] using a simplified optical model is also shown for comparison.

the Rosseland approximation, as illustrated by the reference curves in Fig. 5. While the radiative contribution is negligible at low temperatures, it becomes increasingly significant above approximately 900 K, indicating that radiative heat transfer may contribute appreciably to the overall thermal conductivity under typical thermal barrier coating operating conditions. For $Gd_2Zr_2O_7$, Fig. 5 also compares the present calculations with the radiative thermal conductivity reported by Moskal [28]. The present values are significantly higher than the literature estimates, particularly at elevated temperatures where we see an order of magnitude increase. This difference arises from the treatment of the optical properties within the Rosseland approximation. In the present work, the absorption coefficient and refractive index are evaluated over the full spectral range and their temperature dependence is explicitly accounted for. In contrast, Moskal [28] employed optical properties evaluated at a single wavelength and assumed a constant refractive index. The observed differences therefore highlight the strong sensitivity of radiative heat transport to the underlying thermo-optical properties and underscore the importance of accounting for their spectral and temperature dependence when evaluating high-temperature thermal transport.

As discussed in Section 2.4, the present optical model considers only the phonon-mediated infrared response. The absorption coefficient below 3 μm, where possible electronic contributions to the optical response are not captured by the present model, was therefore approximated, at each temperature, as wavelength-independent and equal to the calculated value at 3 μm. Available experimental optical data [50, 51] indicate low absorption in this spectral region providing qualitative support for the assumed low short-wavelength absorption. A sensitivity analysis was performed by varying the assumed absorption coefficient below 3 μm by ±5% and ±10%, while retaining the calculated optical response at longer wavelengths unchanged. The resulting variation in k_{rad} remains approximately 10% or less over the investigated temperature range, with a maximum deviation of approximately 10.5% at the highest temperature considered for $BaZrO_3$. The complete sensitivity data are provided in the Supplementary Information. The importance of this short-wavelength approximation increases with temperature, as the peak of the blackbody emission spectrum shifts towards shorter wavelengths, resulting in an increasing contribution of the 0.8–3 μm region to the Rosseland integral. The temperature-dependent fractional contribution of the 0.8–3 μm wavelength region to the Rosseland integral is provided in the Supplementary Information for both materials. At elevated temperatures, the electronic contributions to the short-wavelength optical response may become increasingly important; however, their explicit treatment is beyond the scope of the present work.

To examine the conditions under which the optically thick assumption underlying the Rosseland approximation is satisfied, the temperature-dependent absorption-based Rosseland mean extinction coefficient $\beta_R(T)$, photon mean free path, and optical thickness $\tau_R = \beta_R L$ were calculated for representative coating thicknesses of 0.1–0.6 mm for both $BaZrO_3$ and $Gd_2Zr_2O_7$. The results show that the extent to which the optically thick condition is satisfied depends on both coating thickness and temperature, with the condition being more closely approached at larger coating thicknesses. The complete temperature-dependent data are provided in the Supplementary Information.

3.4. Total thermal conductivity

To account for the combined effects of lattice and radiative heat transport, the total thermal conductivity was obtained by summing the radiative contribution, calculated using Eq. (6), and the lattice thermal conductivity obtained from the combined particle and wave-like model using Eq. (2). The resulting total thermal conductivity is compared with the experimental data in Fig. 6. The inclusion of coherent contribution, together with radiative heat transport substantially improves the agreement between the calculated and experimental thermal conductivities, particularly for $Gd_2Zr_2O_7$. While the total lattice contribution alone decreases monotonically with temperature, the addition of the radiative component reproduces the experimentally observed increase in thermal conductivity at high temperatures. These results indicate

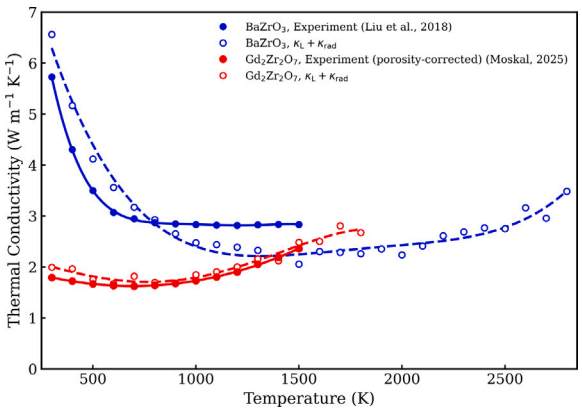

Fig. 6. Calculated total (lattice + radiative) thermal conductivities of $BaZrO_3$ and $Gd_2Zr_2O_7$, compared with experimental results [12,28]. For $Gd_2Zr_2O_7$ the experimental thermal conductivity values are corrected for the reported sample porosity (~10%) using the Klemens relation, as described in Ref. [28]. Symbols represent calculated values and continuous and dashed lines correspond to polynomial fits.

that radiative heat transport constitutes a significant contribution to the overall thermal conductivity of these materials under thermal barrier coating operating conditions.

The improved agreement obtained by combining lattice and radiative heat transport highlights the importance of simultaneously accounting for higher-order phonon scattering, wave-like tunneling of phonon and photon-mediated heat transfer when evaluating high-temperature oxide ceramics. Nevertheless, noticeable differences between the calculated and experimental thermal conductivities remain at the temperatures investigated. These discrepancies may arise from several factors, including electronic heat transport at elevated temperatures [13]. In addition, the experimental measurements may be influenced by microstructural features such as defect populations, and grain-boundary scattering, which are not explicitly accounted for in the present calculations.

4. Conclusion

In this work, the temperature-dependent thermal conductivity of $BaZrO_3$ and $Gd_2Zr_2O_7$ was investigated using a first-principles framework that combines temperature-renormalized phonon properties, three- and four-phonon scattering, coherent phonon transport, and radiative heat transport. The inclusion of four-phonon scattering significantly reduces the predicted particle-like lattice thermal conductivity, demonstrating the importance of higher-order anharmonic interactions in these materials. At elevated temperatures, however, particle-like phonon transport alone is insufficient to reproduce the experimentally observed thermal conductivity. The inclusion of the coherent contribution provides a more complete description of lattice thermal transport and partially compensates for the reduction in the particle-like contribution, with this effect being particularly significant for $Gd_2Zr_2O_7$. However, even after accounting for both particle-like and coherent phonon transport, the calculated lattice thermal conductivity remains lower than the experimentally observed values at elevated temperatures, indicating the increasing importance of an additional heat-transfer mechanism. The calculated radiative contribution increases rapidly with temperature and accounts for a substantial part of this remaining discrepancy. In particular, for $Gd_2Zr_2O_7$, combining the lattice and radiative contributions reproduces the experimentally observed increase in thermal conductivity at high temperatures. The combined treatment of particle-like, coherent, and radiative heat transport therefore provides a more complete description of the temperature-dependent thermal conductivity than a particle-like phonon transport model alone. These results highlight the importance of simultaneously accounting for higher-order phonon scattering, coherent phonon transport, and radiative heat transfer when evaluating high-temperature oxide ceramics for thermal barrier coating applications.

CRediT authorship contribution statement

Harish Kumar: Writing – original draft, Methodology, Investigation, Data curation. **Sreerag Sundaram:** Writing – original draft, Methodology, Investigation, Data curation. **Ankit Jain:** Writing – review & editing, Validation, Supervision, Software. **Karthik Sasihithlu:** Writing – review & editing, Writing – original draft, Visualization, Validation, Supervision, Investigation, Conceptualization.

Declaration of competing interest

The authors declare that they have no known competing financial interests or personal relationships that could have appeared to influence the work reported in this paper.

Acknowledgments

The authors are thankful for the student financial support provided by the Ministry of Education, Government of India. The calculations are carried out on PARAMRUDRA supercomputer facility at IIT Bombay.

S.S. acknowledges financial support from SERB for his award [SB/S9/Z-03/2017-XXIII (2022)] under the Overseas Visiting Doctoral Fellowship (OVDF) program at Purdue University, West Lafayette, USA. S.S. also acknowledges support from Prime Minister's Research Fellowship (PMRF).

Appendix A. Supplementary data

Supplementary material related to this article can be found online at https://doi.org/10.1016/j.ijheatmasstransfer.2026.129679.

Data availability

A subset of the data used in the calculations is available in the Supplementary Information.

References

[1] D.R. Clarke, S.R. Phillpot, Thermal barrier coating materials, Mater. Today 8 (6) (2005) 22–29.
[2] A.K. Rai, M.P. Schmitt, R.S. Bhattacharya, D. Zhu, D.E. Wolfe, Thermal conductivity and stability of multilayered thermal barrier coatings under high temperature annealing conditions, J. Eur. Ceram. Soc. 35 (5) (2015) 1605–1612.
[3] J. Plummer, Understanding a way to fly high, Nat. Mater. 15 (8) (2016) 819–820.
[4] D.R. Clarke, M. Oechsner, N.P. Padture, Thermal-barrier coatings for more efficient gas-turbine engines, MRS Bull. 37 (10) (2012) 891–898.
[5] G. Witz, M. Schaudinn, J. Sopka, T. Buecklers, Development of advanced thermal barrier coatings with improved temperature capability, J. Eng. Gas Turbines Power 139 (8) (2017) 081901.
[6] N.P. Padture, Advanced structural ceramics in aerospace propulsion, Nat. Mater. 15 (8) (2016) 804–809.
[7] R. Vassen, X. Cao, F. Tietz, D. Basu, D. Stöver, Zirconates as new materials for thermal barrier coatings, J. Am. Ceram. Soc. 83 (8) (2000) 2023–2028.
[8] W. Ma, D.E. Mack, R. Vaßen, D. Stöver, Perovskite-type strontium zirconate as a new material for thermal barrier coatings, J. Am. Ceram. Soc. 91 (8) (2008) 2630–2635.
[9] P.S. Murti, M. Krishnaiah, Investigation of the thermal conductivity of calcium cerate and calcium zirconate, Mater. Chem. Phys. 31 (4) (1992) 347–350.
[10] G. Lan, B. Ouyang, J. Song, The role of low-lying optical phonons in lattice thermal conductance of rare-earth pyrochlores: A first-principle study, Acta Mater. 91 (2015) 304–317.
[11] X. Cao, R. Vassen, D. Stöver, Ceramic materials for thermal barrier coatings, J. Eur. Ceram. Soc. 24 (1) (2004) 1–10.

[12] Y. Liu, W. Zhang, B. Wang, L. Sun, F. Li, Z. Xue, G. Zhou, B. Liu, H. Nian, Theoretical and experimental investigations on high temperature mechanical and thermal properties of BaZrO3, Ceram. Int. 44 (14) (2018) 16475–16482.

[13] J. Zheng, D. Shi, Y. Yang, C. Lin, H. Huang, R. Guo, B. Huang, Anharmonicity-induced phonon hardening and phonon transport enhancement in crystalline perovskite $BaZrO_3$, Phys. Rev. B 105 (22) (2022) 224303.

[14] R. Vaßen, M.O. Jarligo, T. Steinke, D.E. Mack, D. Stöver, Overview on advanced thermal barrier coatings, Surf. Coat. Technol. 205 (4) (2010) 938–942.

[15] K. Bobzin, N. Bagcivan, T. Brögelmann, B. Yildirim, Influence of temperature on phase stability and thermal conductivity of single-and double-ceramic-layer EB–PVD TBC top coats consisting of 7YSZ, $Gd_2Zr_2O_7$ and $La_2Zr_2O_7$, Surf. Coat. Technol. 237 (2013) 56–64.

[16] A. Iqbal, G. Moskal, Recent development in advance ceramic materials and understanding the mechanisms of thermal barrier coatings degradation, Arch. Comput. Methods Eng. 30 (8) (2023) 4855–4896.

[17] J. Wu, Low thermal conductivity rare-earth zirconate for potential thermal-barrier coating applications, J. Am. Ceram. Soc. 85 (2002) 3–031.

[18] L. Guo, Y. Li, K. Yan, Corrosion behavior of $Gd_2Zr_2O_7$ thermal barrier coatings under Fe-containing environmental sediment attack, J. Adv. Ceram. 13 (4) (2024) 447–462.

[19] C.G. Levi, Emerging materials and processes for thermal barrier systems, Curr. Opin. Solid State Mater. Sci. 8 (1) (2004) 77–91.

[20] J. Che, X. Wang, X. Liu, G. Liang, S. Zhang, Thermal transport property in pyrochlore-type and fluorite-type $A_2B_2O_7$ oxides by molecular dynamics simulation, Int. J. Heat Mass Transfer 182 (2022) 122038.

[21] Z. Shen, G. Liu, Y. Luo, S. Chen, L. He, R. Mu, Thermal property and failure behaviour of Pr doped $Gd_2Zr_2O_7$ thermal barrier coatings, Corros. Sci. 226 (2024) 111641.

[22] L. Guo, B. Li, Y. Cheng, L. Wang, Composition optimization, high-temperature stability, and thermal cycling performance of sc-doped $Gd_2Zr_2O_7$ thermal barrier coatings: Theoretical and experimental studies, J. Adv. Ceram. 11 (3) (2022) 454–469.

[23] N. Virakante, R. Kumar, A. Jain, Ultralow lattice thermal conductivity in Tl-based chalcogenides via rattling-driven phonon localization, Phys. Rev. B 114 (2026) 065202.

[24] S. Kadkhodaei, S. Fattahpour, A. Davariashtiyani, Heat radiation mitigation in rare-earth pyrosilicate composites: A first principles investigation of refractive index mismatch, Ceram. Int. 50 (9) (2024) 15021–15036.

[25] H. Zhou, J. Tiwari, T. Feng, Understanding the flat thermal conductivity of $La_2Zr_2O_7$ at ultrahigh temperatures, Phys. Rev. Mater. 8 (2024) 043804.

[26] J. Tiwari, T. Feng, Accurate prediction of thermal conductivity of Al_2O_3 at ultrahigh temperatures, Phys. Rev. B 109 (2024) 075201.

[27] Y. Yu, F. Guo, H. Cai, X. Zhang, X. Zhao, Low thermal conductivity and thermal radiation of $La_2Zr_2O_7$ ceramics with hierarchical structure above 1000 K, Ceram. Int. 49 (15) (2023) 25875–25885.

[28] G. Moskal, Selection of low and ultra-low thermal conductivity materials for insulating layers of TBC systems in the context of computational materials science opportunities—a review, J. Therm. Anal. Calorim. 150 (10) (2025) 7207–7251.

[29] G. Kresse, J. Furthmüller, Efficient iterative schemes for ab initio total-energy calculations using a plane-wave basis set, Phys. Rev. B 54 (16) (1996) 11169.

[30] G. Kresse, D. Joubert, From ultrasoft pseudopotentials to the projector augmented-wave method, Phys. Rev. B 59 (3) (1999) 1758.

[31] J.P. Perdew, A. Ruzsinszky, G.I. Csonka, O.A. Vydrov, G.E. Scuseria, L.A. Constantin, X. Zhou, K. Burke, Restoring the density-gradient expansion for exchange in solids and surfaces, Phys. Rev. Lett. 100 (13) (2008) 136406.

[32] H.J. Monkhorst, J.D. Pack, Special points for Brillouin-zone integrations, Phys. Rev. B 13 (12) (1976) 5188.

[33] S.L. Dudarev, G.A. Botton, S.Y. Savrasov, C. Humphreys, A.P. Sutton, Electron-energy-loss spectra and the structural stability of nickel oxide: An LSDA+ U study, Phys. Rev. B 57 (3) (1998) 1505.

[34] Y.B. Losovyj, D. Wooten, J.C. Santana, J.M. An, K.D. Belashchenko, N. Lozova, J. Petrosky, A. Sokolov, J. Tang, W. Wang, et al., Comparison of n-type Gd_2O_3 and Gd-doped HfO_2, J. Phys.: Condens. Matter. 21 (4) (2009) 045602.

[35] X. Gonze, C. Lee, Dynamical matrices, Born effective charges, dielectric permittivity tensors, and interatomic force constants from density-functional perturbation theory, Phys. Rev. B 55 (1997) 10355–10368.

[36] F. Knoop, N. Shulumba, A. Castellano, J.P. Alvarinhas Batista, R. Farris, M.J. Verstraete, M. Heine, D. Broido, D.S. Kim, J. Klarbring, et al., TDEP: Temperature dependent effective potentials, J. Open Source Softw. 9 (94) (2024).

[37] N. Shulumba, O. Hellman, A.J. Minnich, Intrinsic localized mode and low thermal conductivity of PbSe, Phys. Rev. B 95 (2017) 014302.

[38] O. Hellman, P. Steneteg, I.A. Abrikosov, S.I. Simak, Temperature dependent effective potential method for accurate free energy calculations of solids, Phys. Rev. B 87 (2013) 104111.

[39] O. Hellman, I.A. Abrikosov, Temperature-dependent effective third-order interatomic force constants from first principles, Phys. Rev. B 88 (2013) 144301.

[40] A.H. Romero, E.K.U. Gross, M.J. Verstraete, O. Hellman, Thermal conductivity in PbTe from first principles, Phys. Rev. B 91 (2015) 214310.

[41] M. Simoncelli, N. Marzari, F. Mauri, Unified theory of thermal transport in crystals and glasses, Nat. Phys. 15 (8) (2019) 809–813.

[42] M. Simoncelli, N. Marzari, F. Mauri, Wigner formulation of thermal transport in solids, Phys. Rev. X 12 (2022) 041011.

[43] Z. Han, X. Yang, W. Li, T. Feng, X. Ruan, FourPhonon: An extension module to ShengBTE for computing four-phonon scattering rates and thermal conductivity, Comput. Phys. Comm. 270 (2022) 108179.

[44] W. Li, J. Carrete, N.A. Katcho, N. Mingo, ShengBTE: A solver of the Boltzmann transport equation for phonons, Comput. Phys. Comm. 185 (6) (2014) 1747–1758.

[45] Z. Guo, Z. Han, D. Feng, G. Lin, X. Ruan, Sampling-accelerated prediction of phonon scattering rates for converged thermal conductivity and radiative properties, npj Comput. Mater. 10 (1) (2024) 31.

[46] A.J. McGaughey, A. Jain, H.-Y. Kim, B. Fu, Phonon properties and thermal conductivity from first principles, lattice dynamics, and the Boltzmann transport equation, J. Appl. Phys. 125 (1) (2019).

[47] S. Sundaram, Z. Guo, D. Feng, K. Sasihithlu, X. Ruan, First-principles prediction of infrared optical properties of insulators using a resonant photon-phonon interaction model, 2026, arXiv:2606.13143 [cond-mat.mtrl-sci].

[48] K. Parlinski, Lattice dynamics: Vibrational modes, in: F. Bassani, G.L. Liedl, P. Wyder (Eds.), Encyclopedia of Condensed Matter Physics, Elsevier, Oxford, 2005, pp. 98–102.

[49] K. Trachenko, B. Monserrat, M. Hutcheon, C.J. Pickard, Upper bounds on the highest phonon frequency and superconducting temperature from fundamental physical constants, J. Phys.: Condens. Matter. 37 (16) (2025) 165401.

[50] L. Wang, M. Habibi, J.I. Eldridge, S. Guo, Infrared radiative properties of plasma-sprayed $BaZrO_3$ coatings, J. Eur. Ceram. Soc. 34 (15) (2014) 3941–3949.

[51] L. Wang, J.I. Eldridge, S. Guo, Thermal radiation properties of plasma-sprayed Gd2Zr2O7 thermal barrier coatings, Scr. Mater. 69 (9) (2013) 674–677.

[52] M. Huang, Y. Feng, Y. Cheng, X. Liu, W. Pan, C. Wan, Low infrared spectrum transmittance of $Gd_2Zr_2O_7$ through the introduction of a secondary Pt phase, Ceram. Int. (2025).

[53] H.-B. Xu, C.-Y. Zhu, L. Tian, Z.-Y. Li, Applicable scope of the Rosseland model in predicting the radiative thermal conductivity of silica aerogel, Int. J. Therm. Sci. 215 (2025) 109953.

[54] B. Mandal, A. Banerji, V. Sathe, S. Deb, A. Tyagi, Order–disorder transition in $Nd_{2-y}Gd_yZr_2O_7$ pyrochlore solid solution: an X-ray diffraction and Raman spectroscopic study, J. Solid State Chem. 180 (10) (2007) 2643–2648.

[55] D.-H. Gim, Y. Sur, Y.H. Lee, J.H. Lee, S. Moon, Y.S. Oh, K.H. Kim, Pressure-dependent structure of BaZrO3 crystals as determined by Raman spectroscopy, Materials 15 (12) (2022).